# Tailoring the near-surface environment of Rh single-atom catalysts for selective $CO_2$ hydrogenation

Alexander H. Jenkins [a]; Erin E. Dunphy [a]; Michael F. Toney [a, b, c]; Charles B. Musgrave [a]; J. Will Medlin [a]*

[a] Department of Chemical & Biological Engineering; [b] Materials Science & Engineering Program; [c] Renewable and Sustainable Energy Institute

University of Colorado Boulder, 3415 Colorado Avenue, Boulder, Colorado 80303, United States

Abstract:

We used a combination of experimental spectroscopies, density functional theory calculations, and $CO_2$ hydrogenation studies to investigate the effects of modifying single-atom $Rh_1/TiO_2$ catalysts with functionalized phosphonic acid monolayers. We found that deposition of specific amine-functionalized ligands resulted in an ~8× increase in site-specific $CO_2$ reduction turnover frequency at 150 °C and a ~2× increase at 250 °C. On-stream stability also improved following ligand deposition. The effect of the modifier on reactivity was highly sensitive to the proximity of the amine functional group to the surface, which was controlled by adjusting the length of the phosphonic acid tail. Furthermore, deposition of alkyl phosphonic acids without an amine functional group resulted in blocked $CO_2$ adsorption and a near-complete loss of catalytic activity. Infrared spectroscopy studies suggested that the amine group provided binding sites for $CO_2$ that enabled hydrogenation when the amine was positioned near a $Rh_1$ site. Phosphonic acid-modified catalysts also exhibited high selectivity to CO over the series product methane; the selectivity effect was traced to modification of the $Rh_1$ sites to favor CO desorption. Phosphonic acid deposition resulted in an 80-90% loss in accessible $Rh_1$ sites, likely due to blocking by tail groups. However, even with the loss of sites, under low-temperature reaction conditions the rates of $CO_2$ hydrogenation were improved with the coatings, indicating that the remaining sites are highly efficient. Organic functionalization of the supports for atomically dispersed catalysts offers the opportunity to precisely control the positioning of functional groups in the vicinity of a well-defined active site, potentially enabling an additional level of control over active site design.

***Keywords****: $CO_2$ reduction, bifunctional catalyst, self-assembled monolayers, selectivity promoters, atomically dispersed catalyst.*

## 1. INTRODUCTION

For years, supported noble metals have been among the most widely used catalytic materials across many industries.[1–4] However, such catalysts have inherent limitations, including the often

inefficient use of precious metals. Moreover, the linear scaling of adsorption strengths on metal surfaces (linear scaling relations, LSRs) creates a theoretical ceiling for catalytic rates on metal surfaces.[5,6] One route toward circumventing the inherent constraints imposed by LSRs while improving atom efficiency is to use atomically dispersed metals on oxide supports, also known as single-atom catalysts (SACs).[6,7] SACs have recently seen a surge in interest, largely due to their highly efficient use of expensive noble metals.[8] They also provide an attractive platform for tailoring the environment of the SAC to precisely define the active site structure. For instance, they can hypothetically be located adjacent to other types of active sites to enable circumvention of LSRs.[9–11] Another method for tailoring the active site structure and resulting reactivity of SACs is via the deposition of organic ligands.

Deposition of organic monolayers onto metal oxide supports for metal nanoparticle catalysts can improve resistance to metal sintering as well as add bifunctionality. For example, Zhang et al. demonstrated that the deposition of phosphonic acids (PAs) on $Pt/Al_2O_3$ introduced tunable acid sites at the metal–support interface, facilitating hydrodeoxygenation.[12] Zhang also showed that amine-functionalized PAs improved conversion and selectivity for the reverse water-gas shift (RWGS) reaction on $Pt/TiO_2$.[13] Here, the PAs were proposed to have a tandem effect where electron-withdrawal from the metal nanoparticles (NPs) through the support lowered the binding energy of CO to the metal and interactions with the ligands' terminal amines promoted $CO_2$ adsorption at the metal–support interface.

Although deposition of monolayers onto supports has shown promise for controlling reactivity at the nanoparticle-support interface, there are limitations with such systems. The active sites are often poorly defined. Furthermore, the influence of the metal-support interface on reactivity decreases with nanoparticle size as the fraction of active sites near the interface decreases.[14] Modification of SACs with organic monolayers potentially overcomes these challenges, and in fact may allow the synthesis of a new class of molecular catalysts, in which single metal atoms are surrounded by tunable ligands that can change the chemical environment of the active site, not unlike the amino acid residues that surround the active site of an enzyme.

Recently, PA monolayers have been applied to SACs in order to improve catalyst stability and alter adsorbate binding. Modification of $Rh_1/Al_2O_3$ and $Rh_1/TiO_2$ SACs with methylphosphonic acid ($C_1$PA) improved the sintering resistance of these catalysts without appreciably changing the reaction rate of 1-hexene hydrogenation.[15] In addition, Zakem et al. demonstrated that the deposition of octylphosphonic acid on $Rh_1/Al_2O_3$ SACs increased the desorption entropy of CO by restricting the movement of $Rh_1(CO)_2$ species on the oxide surface.[16] While the presence of PAs led to significant improvements in ethylene hydroformylation rates, these ligands also appeared to block 80-90% of available $Rh_1$ active sites. Both studies focused on the steric, geometric, and electronic effects PA monolayers have on SACs. Relatively unexplored, however, is the addition of functionalized ligands to SACs that introduce additional adsorption sites near the $Rh_1$ active site.

The primary goal of this work was to investigate whether amine-functionalized PA monolayers could be tailored to control RWGS activity on $Rh_1/TiO_2$ SACs. Here, our focus was to determine how controlling the position of the amine relative to the catalyst surface (via adjustment of ligand

length and functionality) affected activity, selectivity, and stability (Scheme 1). We show here that while alkyl PAs completely deactivated the catalyst, aminoethyl PA ($C_2NH_2PA$) led to improved RWGS turnover frequencies relative to the uncoated catalysts. Interestingly, amine-functionalized PAs with tails longer or shorter than $C_2$ were much less effective at improving catalytic performance, indicating a high degree of sensitivity to the position of the amine group relative to the Rh active site that appears to be unique to single atom catalysts.

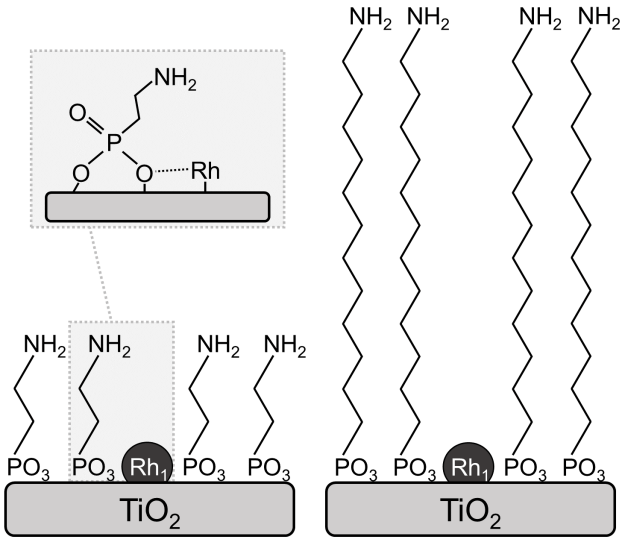


*Scheme 1. Proposed scheme showing a single-atom $Rh_1$ site surrounded by amine-functionalized PA ligands on $TiO_2$ support. Ligand tail length determines the proximity between $Rh_1$ sites and the ligands' terminal amino groups.*

## 2. METHODS

### *2.1. Catalyst synthesis*

#### 2.1.1. Atomically dispersed $Rh_1/TiO_2$

Atomically dispersed Rh on anatase $TiO_2$ was synthesized using the strong electrostatic adsorption technique (adapted from DeRita et al.)[17] at a weight loading of 0.1 wt%. Anatase $TiO_2$ nanopowder (5 nm, US Research Materials, US3838) was sieved at 80 μm to remove any agglomerates and dried overnight before dilution in a 3:1 mixture of $NH_4OH$ solution (28 – 30%, reagent, ACS) and $H_2O$ to target a pH of 9. A 1 mL quantity of $NH_4OH/H_2O$ solution was used for every 10 mg $TiO_2$. $RhCl_3$ (Sigma Aldrich, 98%, 307866) precursor was dissolved in $NH_4OH$ solution at 0.01 M. This precursor solution was further diluted to achieve desired Rh loadings and loaded into a 10 mL syringe pump. Precursor was pumped into the well-mixed $NH_4OH/H_2O/TiO_2$ solution at ambient conditions over 20 hours to form monodisperse Rh sites on the $TiO_2$ surface. After 20 hrs, the resultant mixture was dried under vacuum at 70 °C overnight and then calcined in 20% $O_2$ for 4 hours at 350 °C.

#### 2.1.2. Deposition of organophosphonic acids

While multiple PA SAMs were used in this study, all were deposited following the same steps. A ~3× excess of methylphosphonic acid ($C_1$PA) (Alfa Aesar, 98%, A12619), propylphosphonic acid ($C_3$PA) (Sigma Aldrich, 95%, 305695), aminomethylphosphonic acid ($C_1NH_2$PA) (Thermo Scientific, 99%, L09833), aminoethylphosphonic acid ($C_2NH_2$PA) (Sigma Aldrich, 99%, 268674), aminopropylphosphonic acid ($C_3NH_2$PA) (AmBeed, 98%, A172849), or aminododecylphosphonic acid ($C_{12}NH_2$PA) (SiKÉMIA, 95%, SIK7701-10) was dissolved in tetrahydrofuran (for alkyl PAs) or $H_2O$/ethanol (for amino-PAs). $Rh_1/TiO_2$ catalyst was reduced in 20% $H_2$/Ar at 100 °C for 4 hours, then immediately added to the PA solution. Stirring was maintained for 12 h, then the resultant suspension was separated with centrifugation and annealed in air at 120 °C for 6 h. Following annealing, the solid powder was re-suspended in the tetrahydrofuran or water and centrifuged to remove weakly adsorbed PAs. This wash was repeated 5 times before finally drying the sample under vacuum at ambient temperature. This treatment has been found to produce PA-saturated $TiO_2$, with surface densities of approximately 3 $nm^{-2}$. An exception is $C_1$PA, which yields surprisingly high P loadings suggesting a surface coverage near 6 $nm^{-2}$.[13,18]

*2.2. Material characterization*

Fourier-transform infrared (FTIR) spectra were recorded using a Thermo Fisher Scientific Nicolet 6700 FTIR (100 scans at a resolution of 4 $cm^{-1}$). A closed cell attachment (Harrick) was used for CO-probe-molecule and $CO_2$-probe-molecule diffuse reflectance infrared Fourier transform spectroscopy (DRIFTS). Samples were reduced at 150 °C (unless otherwise noted) using 20% $H_2$/Ar, then cooled to 50 °C in Ar. Following background collection at 50 °C in Ar, 10% CO/He was introduced to the cell for 15 min. Then, flow was switched back to pure Ar and sample scans were taken every 2 min for a total of 30 min as CO was purged from the system. For in-situ RWGS DRIFTS experiments, catalysts were reduced in-situ before setting the total flowrate to 250 sccm with a $CO_2$:$H_2$:Ar ratio of 1:5:19. Catalyst loading for all DRIFTS experiments was ~30 mg.

X-ray adsorption spectra (XAS) at the Rh K-edge (23219 eV) were measured at beamline 5-ID-D at the Advanced Photon Source (APS, 7 GeV, 100 mA, monochromatized with Si (111) double-crystals, detuned to ~55%). Reference and experimental spectra for Rh foil, $RhCl_3$, 0.5 wt% $Rh_1/TiO_2$, and 0.5 wt% $Rh_1/TiO_2$@$C_2NH_2$PA catalysts were recorded in transmission mode using ionization chambers. Powdered catalyst (40 mg), prepared as previously described, was loaded into quartz capillaries (0.2 mm wt., 1/8" O.D.) with open ends and capped with quartz wool. The average packing density for each sample was 0.1 $mg/mm^3$. Capillaries were then loaded into a custom XAS reactor (see Supporting Information) and reduced with 1 bar of 3% $H_2$/He at 100 °C for 30 minutes. Following reduction, the temperature was decreased to 60 °C, and 3% $H_2$/He pressure was maintained. Three scans were then collected for each sample with a beam size of 5 $mm^2$. Additional methods and analysis for XAS acquisition, normalization, and fitting are provided in the Supporting Information (SI).

*2.3. Vapor-phase reactions*

Hydrogen-deuterium exchange reactions ($H_2/D_2$ scrambling) were conducted to probe the catalytic active surface area for hydrogenation before and after modification with PAs. A 25 mg quantity of Rh SAC catalyst was loaded into a continuous flow packed bed ambient pressure reactor. Samples were reduced in-situ in 20% $H_2$/Ar at 150 °C, then cooled to 30 °C. Doses of $D_2$ (1.0 mL per dose; Sigma Aldrich, 99.8%, 361860) were injected via syringe into the feed stream, and conversion to HD was analyzed with a Pfeiffer Vacuum Prisma 80 quadrupole mass spectrometer. Due to high excess of $H_2$ in the feed stream, $D_2$ conversions >99% were observed for samples with excessively high catalyst loadings, while no conversion of $D_2$ was measured on bare $TiO_2$.

Catalytic performance for RWGS reactions was analyzed in a continuous flow packed bed reactor at ambient pressure. Before reaction, samples were reduced at either 150 or 250 °C for 30 min, then cooled to ambient temperatures. For RWGS reactions, total feed rate was set to 25 sccm, with a $CO_2$:$H_2$:He ratio of 1:5:19. After establishing flow rates, the reactor was heated from ambient temperature to either 150 or 250 °C at a rate of ~40 °C/min. Reaction products were analyzed online using both a Pfeiffer Vacuum Prisma 80 quadrupole mass spectrometer and an SRI Instruments 8610C gas chromatograph equipped with a Hayesep D column, thermal conductivity detector, and flame ionization detector.

### *2.4. DFT calculations*

Quantum mechanical calculations were performed using plane wave periodic boundary condition density functional theory (DFT) as implemented in the Vienna Ab initio Simulation Package (VASP).[19–22] DFT calculations employed the Strongly-Constrained and Appropriately-Normed (SCAN) exchange correlation functional coupled with projector augmented wave (PAW) pseudopotentials with a cutoff energy of 400 eV.[23,24] The anatase $TiO_2$ (101) surface was modelled with 4×2×3 supercell slabs separated with 20 Å of vacuum. Ti and O atoms in the bottom two layers were fixed in their bulk positions. A Γ-centered Monkhorst−Pack 3×3×1 grid was utilized for slab calculations. Geometry optimizations were considered converged when all forces were < 0.01 eV/Å and self-consistent field calculations converged when the energy changes between electronic steps were < -0.002 eV. The effective charge of each atom was estimated using the Bader approach as implemented by Henkelman et al.[25]

## 3. RESULTS AND DISCUSSION

### *3.1. Catalyst Synthesis and DRIFTS Characterization*

$Rh_1/TiO_2$ was synthesized via strong electrostatic adsorption at a loading of 0.10 wt%. To confirm that adsorbed Rh was atomically dispersed, CO probe molecule DRIFTS was utilized. Stretches at ~2,025 and ~2,090 $cm^{-1}$ were observed following the exposure of $Rh_1/TiO_2$ to CO (Figure 1). These were assigned to symmetric and asymmetric stretches of Rh gem-dicarbonyl species, $Rh_1(CO)_2$. Previous IR spectroscopy studies of alumina-supported Rh have thoroughly demonstrated these gem-dicarbonyl stretches as unique to isolated $Rh_1$ sites.[26,27]

To demonstrate the difference in C-O stretching modes between Rh particles and $Rh_1$ sites, $Rh_1/TiO_2$ was exposed to $H_2$ at elevated temperatures. Rh adatoms have been shown to be highly mobile, particularly at elevated temperatures and reducing conditions, leading to the formation of

Rh particles and the loss of $Rh_1$ sites under common reaction conditions.[28,29] In-situ reductions in 20% $H_2$/Ar were performed at 100, 200, and 300 °C for one hour, followed by CO DRIFTS. Figure 1 shows the growth of a peak at ~2,050 $cm^{-1}$ following reduction at 300 °C, which was assigned to linearly bound CO on Rh particles, indicating Rh sintering had occurred.[30] Following reduction at 200 °C, DRIFT spectra showed minor absorbance at ~2,050 $cm^{-1}$ as the signal failed to return to the baseline, suggesting a significant degree of sintering.

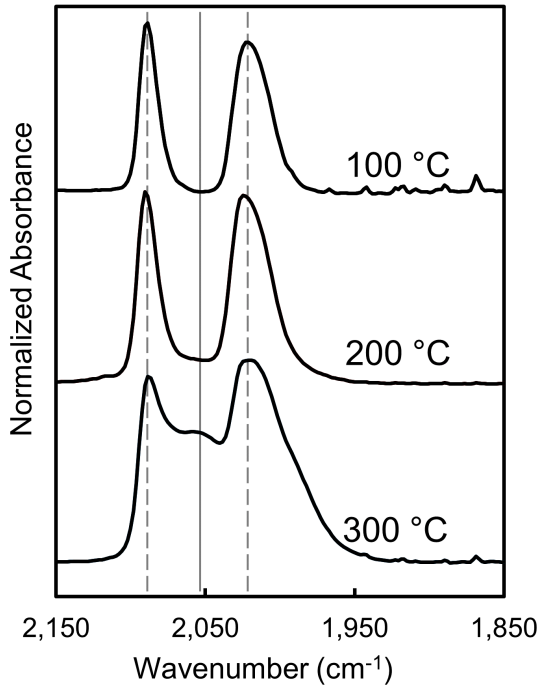


*Figure 1.* ***Conversion of $Rh_1$ species to nanoparticles by annealing****. CO DRIFT spectra for $Rh/TiO_2$ following 1 hour in-situ reduction at the indicated temperatures. Stretches at ~2,025 and ~2,090 $cm^{-1}$ (dashed lines) are assigned to $Rh_1(CO)_2$ species. The stretch at ~2,050 $cm^{-1}$ (solid line) is assigned to linear CO adsorption on Rh particles.*

Following the synthesis of $Rh_1/TiO_2$, PA self-assembled monolayers (SAMs) were deposited onto the catalyst. $C_2NH_2PA$ and $C_3PA$ were chosen initially to allow comparison of alkyl and amine-functionalized ligands of a similar size. The presence of these SAMs on the catalyst surface was confirmed with DRIFTS by the observed C-H stretches shown in Figure S1 of the SI.[31] In addition to studying Rh SACs modified with $C_2NH_2PA$ and $C_3PA$, we also investigated $C_3PA$-modified catalysts where the ligands' organic tails were removed via oxidation at 400 °C, which we will refer to as $C_3PA$-ox. Previous studies have shown this treatment to remove PA tail groups, while even 700 °C treatments in air had no significant effect on phosphorus loading for PAs bound to $TiO_2$.[32] $^{31}P$ NMR was conducted on $C_1PA$-modified $TiO_2$ in order to elucidate the nature of the PA head groups following this oxidative treatment (Figure S2). The observed upfield shift following oxidation is consistent with better shielding of the P center, with the oxidized sample resembling phosphoric acid bound to $TiO_2$.[33,34] This suggests that the PA's P–C bonds are replaced with P–O bonds during tail removal.

CO DRIFTS was performed on PA-modified $Rh_1/TiO_2$ samples to investigate the effect of PA deposition on Rh dispersion. Figure 2a shows normalized C-O stretching regions for each catalyst sample. CO stretches related to the Rh gem-dicarbonyl were observed, confirming that $Rh_1$ sites were still accessible following the addition of PAs, whereas the lack of linear-bound C–O stretches indicated that Rh clusters did not form during PA deposition. Additionally, $Rh_1(CO)_2$ stretches on the PA-modified samples were redshifted ~10 $cm^{-1}$. In the study by Zakem et al, the addition of octylphosphonic acid to $Rh_1/Al_2O_3$ resulted in a similar redshift, which was attributed to through-space interactions between adsorbed CO and the PA SAMs.[16] Notably, the extent and direction of the CO frequency shift was sensitive to the functional groups on the PA tail, with fluorinated groups on PA modifiers producing a blueshift.[16]

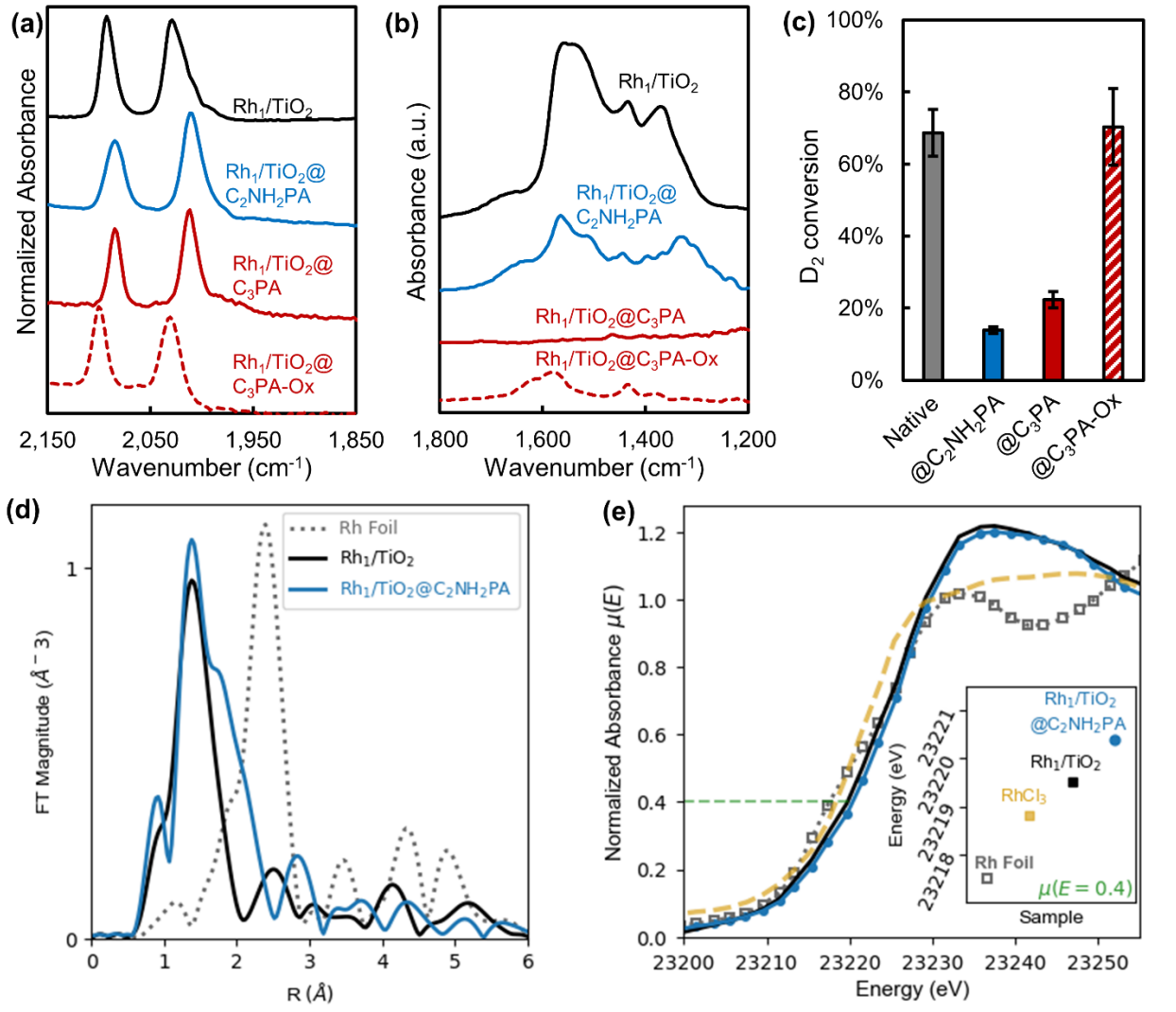


*Figure 2.* ***SAC Characterization*** *(a) CO DRIFTS and (b) $CO_2$ DRIFTS spectra for unmodified and PA-modified $Rh_1/TiO_2$. Measurements were taken at 50 °C after flowing dilute $CO/CO_2$ over samples for 15 minutes, followed by a 3-minute purge in pure Ar to remove vapor-phase $CO/CO_2$. (c) $D_2$ conversion to HD during $H_2/D_2$ scrambling experiments for PA-modified and unmodified $Rh_1/TiO_2$. $D_2$ was introduced by 1*

*mL injections while flowing constant 20% $H_2$/Ar. (d) Magnitude of Fourier transform performed on $k^2$-weighted χ(k) function of the EXAFS spectra for the Rh K-edge of Rh foil, $Rh_1/TiO_2$, and $Rh_1/TiO_2$@$C_2NH_2PA$. It should be noted that the Rh foil EXAFS has been scaled by a factor of 1/3 for comparison. (e) XANES of Rh foil (gray), $RhCl_3$ (gold), $Rh_1/TiO_2$ (black), and $Rh_1/TiO_2$ @$C_2NH_2PA$ (blue). The inlaid plot shows the threshold energy values (when the normalized intensity is 0.4).*

The state of $Rh_1/TiO_2$ during the formation of PA monolayers had a significant impact on the accessibility of Rh. Samples that were reduced immediately prior to the addition of PAs showed CO stretching peaks ~17× larger than those that were oxidized prior to SAM deposition (Figure S3). Tang et al. showed that $Rh_1$ species migrate into rutile $TiO_2$ cation vacancies and form $Rh^{4+}$ during oxidative treatments and are unable to adsorb CO in this state.[35] We hypothesize that PA monolayers "lock in" these Rh cations, keeping them inaccessible even after subsequent reduction in $H_2$. We therefore generally prepared materials via reducing the catalyst prior to phosphonate deposition.

The effect of PA-modification on $CO_2$ uptake was investigated with $CO_2$ probe molecule DRIFTS. Figure 2b shows the stretching region for adsorbed $CO_2$ on each sample. The primary observed peaks for unmodified $Rh_1/TiO_2$ were assigned to the asymmetric and symmetric stretching of monodentate carbonates (1,560 $cm^{-1}$ and 1,370 $cm^{-1}$, respectively) and to monodentate bicarbonates (1,430 $cm^{-1}$), indicating $CO_2$ was chemically adsorbed to the oxide.[36] No $CO_2$ uptake was observed following the addition of $C_3PA$, consistent with the elimination of $TiO_2$ adsorption sites by PA head groups. Stretches were observed in this region, however, for the $C_2NH_2PA$-modified sample, suggesting that the terminal amine group of $C_2NH_2PA$ is capable of adsorbing $CO_2$. These peaks were assigned to carbamate asymmetric (1,560 $cm^{-1}$) and symmetric (1,440 $cm^{-1}$ and 1,370 $cm^{-1}$) stretches, $NH_3^+$ deformation modes (1,640 $cm^{-1}$ and 1,520 $cm^{-1}$), and $NCOO^-$ skeletal vibrations (1,400 $cm^{-1}$ and 1,320 $cm^{-1}$).[37,38] The area of the $CO_2$ stretching peaks is ~2× larger for the native $Rh_1/TiO_2$ than for the $C_2NH_2PA$-modified sample; we attribute this reduction in intensity to these PAs only introducing one $CO_2$ binding site while occupying 2 or 3 adsorption sites on the $TiO_2$ surface. $CO_2$ adsorption was also observed on $Rh_1/TiO_2$@$C_3PA$-ox, suggesting that surface modified with oxidized PA head groups can bind $CO_2$ as well, consistent with studies on other titanium phosphonates.[39,40] For this sample, the $CO_2$ stretching peak areas were ~6× smaller than on the native sample, likely due to a lower density of $CO_2$ adsorption sites on the catalyst surface.

### *3.2. X-ray Absorption Spectroscopy*

We utilized XAS at the Rh K-edge to confirm the deposition of atomically dispersed Rh and identify changes to the catalyst's local binding environment following the deposition of $C_2NH_2PA$. Methods and analysis for the acquisition, normalization, and fitting are provided in the SI.

To confirm that Rh was atomically dispersed on both the unmodified and PA-modified samples, we turned to extended X-ray absorption fine structure (EXAFS). Comparing the EXAFS Fourier transform profiles for the Rh foil, $Rh_1/TiO_2$, and $Rh_1/TiO_2$@$C_2NH_2PA$ in Figure 2d, it is evident that there are distinct differences between the Rh foil standard and the $Rh_1/TiO_2$ catalyst samples in the range of 1–4 Å. Rh foil peaks at 2.7 and 3.8 Å correspond well to first and second shell Rh-Rh bonding, respectively. While the 2.7 Å Rh-Rh peak dominates the foil standard, the

dominant feature of the $Rh_1$ samples are at much lower bond lengths, consistent with their high dispersion. To determine the contributions of scattering paths for the $Rh_1/TiO_2$ catalysts from 1–3.5 Å, DFT-calculated models of the $Rh_1/TiO_2$ and $Rh_1/TiO_2$@$C_1$PA surfaces, shown in Figure 3, were utilized in FEFF[41,42] simulations for EXAFS fitting.

Our approach in the DFT calculations was to use a simple surface model that was based on previous results for Rh adatoms bound on stoichiometric $TiO_2$.[35] It is important to point out that the experimental system has considerable complexity that is not fully captured by the model. For example, the previous work showed that under reducing conditions, it is thermodynamically favorable to form oxygen vacancies that reside under Rh sites.[35] However, prior work on supported nanoparticle systems suggests that O vacancy formation is kinetically limited at the mild reduction temperatures used for the EXAFS pretreatment (100 °C) and data collection (60 °C), i.e. temperatures in excess of 200 °C are generally required to initiate $TiO_2$ reduction from supported metal catalysts.[43,44] The $TiO_2$ surface is also expected to expose various facets and defects. Given the expected complexity of the oxide and recently reported limits on the ability of EXAFS to resolve the precise environment around SACs,[45] we focused on modeling changes to the Rh atom environment for the simplest $TiO_2$ model, hypothesizing that such a system would allow a basic understanding of how PA modifiers alter the environment of Rh adatoms. The FEFF-derived fits for this model, shown in Figure 3e, indicate that the peaks in the range of 1–2 Å are dominated by Rh-O coordination, and the peaks in the range of 2–3 Å are a combination of second shell Rh-Ti and third shell Rh-O coordination. A more rigorous analysis of the fits in Figure 3e is provided in the Supporting Information (SI).

X-ray absorption near-edge spectroscopy (XANES), shown in Figure 2e, indicated qualitatively similar pre-edge, white-line, and multipole profiles for unmodified and $C_2NH_2$PA-modified $Rh_1/TiO_2$. The multipole region (> 23,230 eV) of the catalysts is distinctly different than that of the Rh foil and $RhCl_3$ standards. These differences are associated with the direct transitions of the excited photoelectron into the continuum, and the shapes of these regions compare well to standards in literature.[46] Additionally, the threshold energy (defined here as the energy for which the normalized absorption is 0.4) is higher for the two $Rh_1/TiO_2$ catalysts than Rh foil and $RhCl_3$, with the $C_2NH_2$PA-modified sample higher than the uncoated sample. We interpret the increased threshold energies as indicating increased oxidation of the Rh, consistent with the $RhCl_3$ having an increased threshold energy relative to Rh foil. Thus, we concluded that both $Rh_1/TiO_2$ catalysts have average oxidation numbers greater than three. This is consistent with reports of Rh single atoms supported on $ZrO_2$, $CeO_2$, and $Al_2O_3$, which demonstrated Rh oxidation states between 3+ and 4+.[47-49] The relative increase in threshold energy ($\mu(E) = 0.4$) of the PA-modified catalyst compared to that of the unmodified catalyst indicates that PA deposition results in withdrawal of electron density from the Rh single atoms.[50]

It is interesting to note some of the subtler differences in the transformed EXAFS spectra (Figure 2d) for the unmodified and $C_2NH_2$PA-modified $Rh_1$ catalysts, where there are clear differences in intensity above ~1.8 Å, suggesting differences in the local coordination environment of the Rh atom. To better understand that local environment, we carried out DFT calculations of unmodified and $C_1$PA-modified $Rh_1/TiO_2$ surface models. For the unmodified $TiO_2$ surface,

adjusting initial placement of the Rh adatom resulted in five unique relaxed structures where Rh adsorption to the O–O bridge site was 0.4–0.9 eV stronger than in the other four models, shown in Figure S4. For the modified surface, C1PA ligands were modeled in a bidentate binding mode as suggested by previous experimental findings.[14] Similar to the unmodified $TiO_2$, four unique structures were found for the $Rh_1/TiO_2@C_1PA$ surface, the most stable being 0.1–1.3 eV stronger than the other models (Figure S4).

These DFT calculations showed that, when in the proximity of $C_1PA$, the Rh single atom interacts with the ligand head group to form an Rh–O–P linkage (Figure 3d). In addition, there is an apparent interaction between a Ti-bound O atom of a phosphonate and Rh, with a computed distance of 2.21 Å. This is apparently consistent with experimental EXAFS results, where the coordination number for the first shell of Rh–O increases from 5.2 to 6.6 between $Rh_1/TiO_2$ and $Rh_1/TiO_2@C_2NH_2PA$, although the error bars are sufficiently large (Table S2 and S3) to prohibit a definitive determination. In the DFT calculations, the Bader charge of the Rh single atom, shown in Figure 3, increased by 0.3 $|e^-|$/atom following the addition of $C_1PA$, further indicating that the addition of PAs resulted in a decrease in electron density at the Rh site. It should be noted that the experimental EXAFS results show high degrees of disorder associated with singular scattering paths, likely due to a heterogeneous mix of Rh sites on a variety of $TiO_2$ facets. Additional information for XAS fitting is provided in the SI.

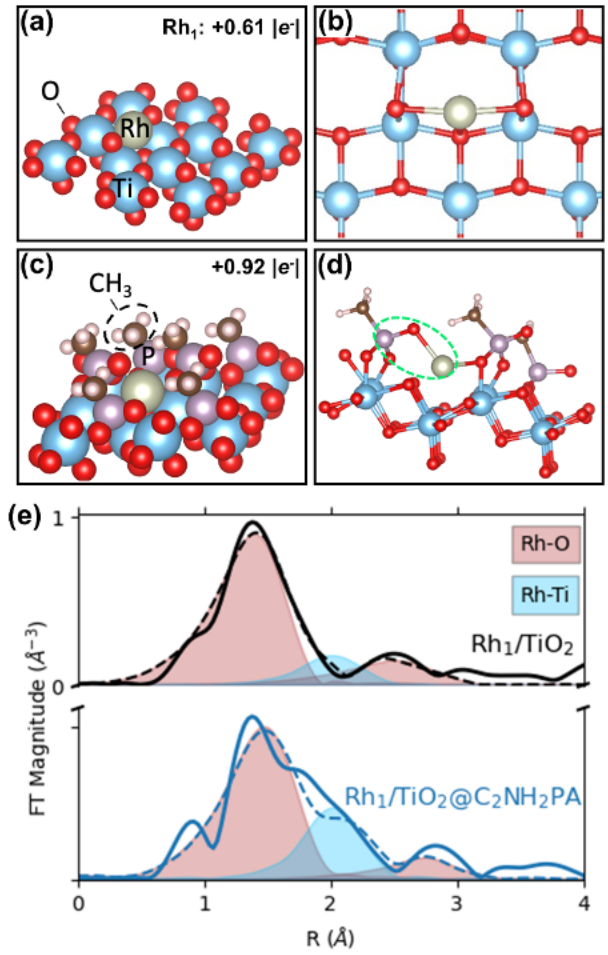


*Figure 3.* ***SAC structural models****. DFT-calculated models of $Rh_1/TiO_2$ (space-filling view a & top-down view b), and of $Rh_1/TiO_2$@$C_1$PA (space-filling view c & side view d) for the $TiO_2$ (101) surface. Panels (a) and (c) show DFT-calculated Bader charges for the $Rh_1$ atom of each structure. Color code: red = O, white = H, blue = Ti, grey = Rh, purple = P, brown = C. (e) Magnitude of Fourier transform (FT) performed on $k^2$-weighted χ(k) function of the EXAFS spectra for the Rh K-edge of $Rh_1/TiO_2$ and $Rh_1/TiO_2$@$C_2NH_2$PA. Solid lines are the experimentally obtained EXAFS profiles and dashed lines show the fitted EXAFS profiles. Filled regions show Rh–-O (red) and Rh–Ti (blue) scattering paths fit from FEFF simulations.*

### *3.3. Effect of PA modification on $H_2/D_2$ Scrambling Rates*

Vapor-phase $H_2/D_2$ scrambling experiments were performed on catalyst samples to determine the extent of site blocking toward hydrogen dissociation /recombination by PA SAMs. Scrambling experiments were conducted at 30 °C by injecting 1 mL doses of $D_2$ while constantly flowing $H_2$ and Ar. Figure 2c shows the conversion of $D_2$ to HD for each catalyst sample. Modification of $Rh_1/TiO_2$ with $C_2NH_2$PA resulted in a decrease in scrambling conversion from 69% to 14%. Assuming the scrambling reaction is first-order in $D_2$,[51] this change in conversion represents a ~8× decrease in available Rh sites following $C_2NH_2$PA deposition. Similarly, $C_3$PA-modified samples demonstrated a ~5× decrease in scrambling rates. This drop in site availability is consistent with the previously noted study by Zakem et al., in which CO pulse chemisorption was used to

determine an 80–90% loss in accessible Rh sites following PA deposition. PA ligands have also been shown to alter or block active sites at the metal-support interface of supported nanoparticle catalysts, such as with CO oxidation on PA-modified $Au/TiO_2$.[32]

The loss of accessible Rh sites is likely due to blocking by the PAs rather than Rh sintering, as linear-bound CO was not observed during CO DRIFTS characterization. In addition, removal of the PA tail groups through oxidation resulted in apparently complete recovery of active sites. The difference in scrambling activity between $C_2NH_2PA$- and $C_3PA$-modified samples, as well as the recovery of activity post-oxidation, suggests that the loss in Rh sites is due to blocking specifically by the PA tail groups. However, it is also possible that the 400 °C oxidation treatment alters the binding conformation of the PA head group, giving access to Rh sites.

One alternative explanation for the lower scrambling activity on PA modified samples is that the presence of phosphonic acids increases the barrier for $H_2$ dissociation, a step assumed to be facile. To test this, $H_2/D_2$ scrambling experiments were performed on the native and $C_2NH_2PA$-modified samples at the elevated temperature of 250 °C. It was found that the calculated percentage of blocked sites dropped from 87% to 84% at these conditions, an insignificant change, suggesting that the lower rates of $H_2/D_2$ scrambling on PA-modified catalysts are indeed due to a loss in accessible Rh sites (Figure S5).

### 3.4 *RWGS reaction studies*

The effects of PA-modification of $Rh_1/TiO_2$ on RWGS catalytic performance were investigated with a temperature-controlled tubular packed bed reactor. Initial reactions were run at 150 °C to maintain atomic dispersion of Rh. $CO_2$, $H_2$, and He were flowed at a 1:5:19 ratio at a total flow rate of 25 sccm. At these conditions, 400 mg of 0.1 Rh wt% catalyst was required to achieve $CO_2$ conversions between 0.5–1.0% (equilibrium conversion at these reaction conditions is ~4%). Figure 4a shows overall $CO_2$ hydrogenation rates based on total Rh loading, i.e., without correcting for the number of accessible sites. Despite extensive site blocking, the $C_2NH_2PA$-modified samples still produced ~50% more CO than the native catalyst. Conversely, modification with $C_3PA$ led to a complete loss of catalytic activity. This is likely due to the blocking of $CO_2$ adsorption sites by the PAs. Similar to $H_2/D_2$ scrambling, the removal of the PA tails via oxidation resulted in recovery of catalytic activity, despite $Rh_1/TiO_2@C_3PA$-ox displaying considerably lower peak areas during $CO_2$ DRIFTS experiments. Additionally, Figure S6 shows the rate of $CO_2$ conversion normalized by the rate of $H_2/D_2$ scrambling on the same catalyst. This normalized rate is used here as an estimate of the accessible-site based $CO_2$ turnover frequency (TOF) for each catalyst, under the assumption that the number of accessible sites is proportional to the scrambling rate. Even if this proportionality is non-linear, TOFs calculated in this way serve to normalize $CO_2$ hydrogenation rates via the rate of key elementary step in the RWGS reaction. Here, modification of $Rh_1/TiO_2$ with $C_2NH_2PA$ resulted in an 8× increase in TOF (as defined in this way) towards CO.

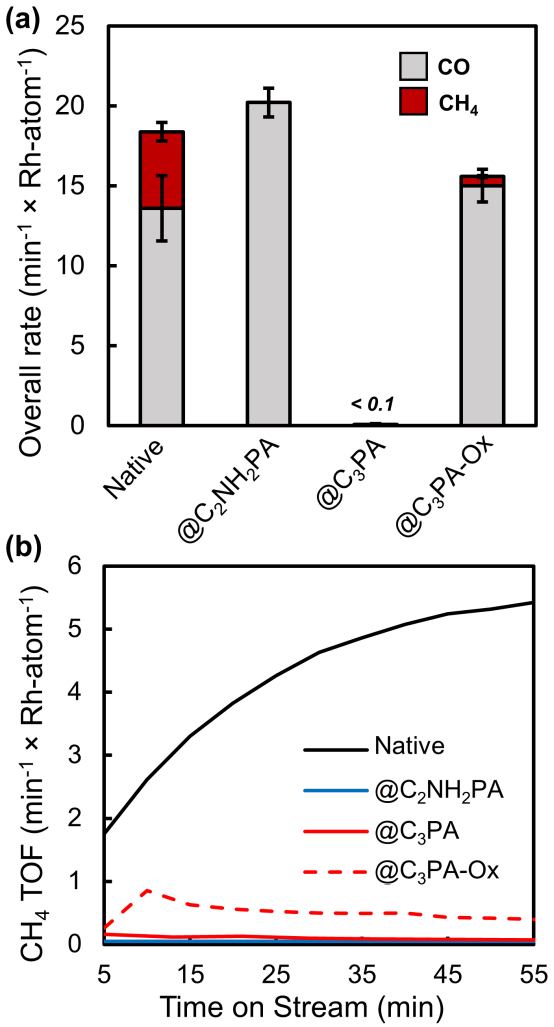


*Figure 4.* ***Low-temperature RWGS performance of SACs****. (a) $CO_2$ reduction rate to CO (green) and methanation rate to $CH_4$ (red), normalized by total Rh loading. (b) Methanation rate vs. time on stream. $CO_2$ reduction experiments were run at 150 °C. $CO_2$ conversion ranged from 0.0–1.0%, while equilibrium conversion for RWGS at these conditions is ~4%.*

Catalyst modification with PAs also reduced the rate of methanation during $CO_2$ reduction. The native, $C_2NH_2PA$-, and $C_3PA$-ox-modified catalyst showed 74, 100, and 96% selectivity to CO, respectively. The formation of methane on unmodified $Rh_1/TiO_2$ was observed to increase during the first ~1 hour of reaction before leveling out (Figure 4b). $CO_2$ methanation can occur directly, or sequentially if CO further hydrogenates before desorbing from the catalyst, and is typically considered irreversible.[52] A study by Matsubu et al. in $H_2$-lean conditions demonstrated the tendency for $Rh_1$ sites to produce CO during $CO_2$ hydrogenation, whereas Rh NPs tended to form $CH_4$.[30] However, post-reaction characterization with CO DRIFTS showed no signs of Rh sintering on either of our catalysts.

Weaker CO binding, as opposed to Rh sintering, was likely responsible for the improvements in RWGS selectivity and low-temperature activity following modification with

amine-functionalized PAs. CO DRIFTS conducted after annealing in flowing Ar to progressively higher temperatures showed that modification of $Rh_1/TiO_2$ with $C_1PA$ resulted in a 50–100 °C lower CO desorption temperature compared to the unmodified catalyst (Figure S7), potentially accounting for the higher rates if the RWGS reaction is CO-desorption limited at 150 °C. Exploratory DFT calculations also showed weaker adsorption of a single CO molecule (by ~0.6 eV) when the $Rh_1/TiO_2$ surface is modified by $CH_3PA$ (Figure S8). The ability for atomic H to adsorb near $Rh_1$ active sites is also likely affected by the presence of PA head groups on the support surface, potentially affecting hydrogenation rates. The stronger adsorption of CO on the native catalyst may also contribute to the higher rate of methanation compared to PA-modified samples, as the probability of sequential hydrogenations increases with higher CO coverage. A similar study conducted by Zhu et al. on $Rh_1/Fe_3O_4$ attributed high $CO_2$ hydrogenation activity as well as high selectivity to CO to strong interactions between Rh–O–Fe sites and $CO_2$, as well as weak interactions with CO.[53]

The weakening of CO adsorption following the deposition of PAs has been demonstrated on $TiO_2$-supported Pd- and Pt-nanoparticle catalysts.[13] In that study, PAs were thought to decrease the CO adsorption energy to metal sites by electron-withdrawal through the support, which affected the metal's ability to bind CO through backdonation to 2 π orbitals. While our model suggests that electron-withdrawal from Rh occurs via Rh–O–P bonds rather than by through-support interactions, the effect on CO adsorption strength may be similar. The effects of $C_8PA$ monolayers on CO desorption from $Rh_1/TiO_2$ have also been observed by Zakem et al.[16] In their study, it was shown that PAs do not significantly affect the enthalpy of desorption, but they do reduce the entropic penalty of the CO desorption transition state by limiting degrees of freedom for the $Rh_1(CO)_2$ initial state.[16] A similar effect likely contributes to weaker CO binding here.

Additional RWGS reaction experiments were carried out at 250 °C under the same flow conditions to explore reactivity closer to relevant process conditions, and where CO desorption is expected to be less limiting. Here, the reactor was loaded with 100 mg of catalyst to achieve conversions up to ~13%; equilibrium conversion at these conditions is ~21%. Figure 5 (left axis) shows the $CO_2$ TOF for each catalyst, where once again $H_2/D_2$ scrambling results were used to calculate the quantity of accessible Rh sites. At this elevated temperature and with a much lower reactor loading, selectivity for all catalysts exceeded 97%. This difference in methanation from the experiments run at 150 °C is again likely due to the facile nature of CO desorption at this elevated temperature.

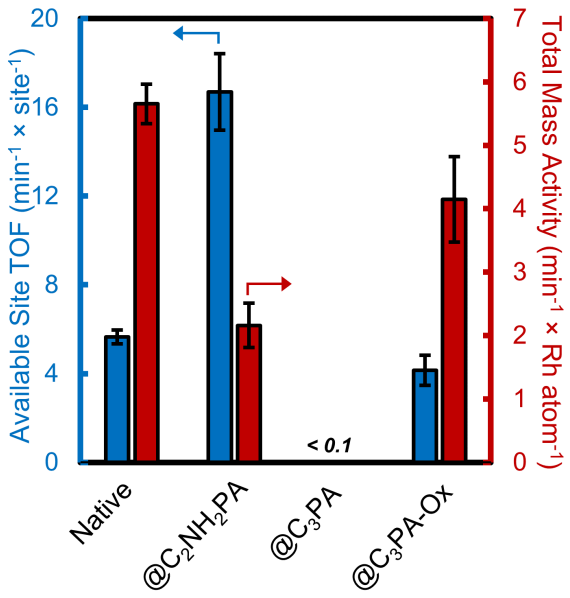


*Figure 5.* ***250 °C RWGS performance of SACs.*** *Turnover frequencies for $CO_2$ reduction to CO based on accessible sites (blue, left axis) and Rh-mass-based activity (red, right axis). $CO_2$ reduction experiments were run at 250 °C. $CO_2$ conversion ranged from 0.0–13%, while equilibrium conversion at these conditions is ~21%.*

Once again, $C_2NH_2PA$-modified catalysts demonstrated the highest rate on an available site basis, a ~2× increase compared to the native sample. However, at these conditions, the improvement in specific rate was not enough to compensate for site blocking, resulting in lower overall $CO_2$ conversion compared to the unmodified catalyst (Figure 5, right axis). Modification with $C_3PA$ resulted again in complete loss of catalytic activity, presumably due to blocked $CO_2$ adsorption. Oxidative removal of tails resulted in the recovery of most, but not all, catalytic activity, as $CO_2$ TOFs on $Rh_1/TiO_2$@$C_3PA$-ox were ~26% lower than those on the native sample.

Though they had lower overall $CO_2$ activities, the PA-modified samples did demonstrate significantly improved on-stream stability compared to native $Rh_1/TiO_2$. Figure S9 shows normalized on-stream RWGS conversion at 250 °C during the first hour of reaction where, after 1 hour on-stream, $CO_2$ conversion on unmodified $Rh_1/TiO_2$ had decreased by 10–20%. We tested this catalyst for ~25 hours on stream at 250°C and found that activity stabilized after ~4 hours at a value of ~85% of the initial activity (see Figure S10). The PA-modified samples saw no such loss in activity; in fact, conversion had increased after 1 hour in most cases. This increase in conversion is unlikely to have been caused by PA tail degradation, as it was also observed for the $C_3PA$-ox-modified samples that had already had their tails groups removed.

To better understand this difference in catalyst stability, samples were characterized with CO DRIFTS immediately following 12 hours of in-situ $CO_2$ reduction at 250 °C (Figure 6). On the native $Rh_1/TiO_2$ sample, prominent growth of the peak associated with linear-bound CO (~2,060 $cm^{-1}$) indicates significant metal sintering; the peak growth is much less for the $C_2NH_2PA$-modified catalyst. This significant reduction in sintering follows previously observed trends, where

it was hypothesized that PA monolayers provide physical diffusion barriers and weaken metal-adsorbate interactions, limiting adsorbate-promoted diffusion.[15]

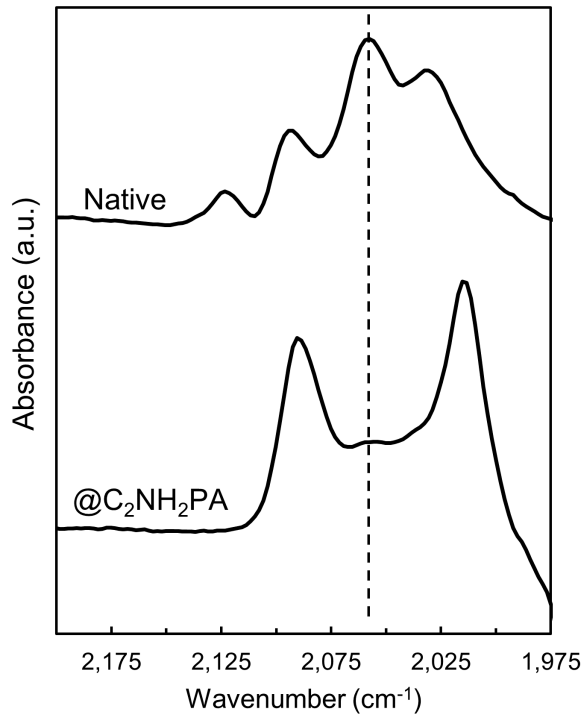


*Figure 6.* ***Impact of PAs on $Rh_1$ stability****. CO DRIFTS of $Rh_1/TiO_2$ and $Rh_1/TiO_2$@$C_2NH_2PA$ following in-situ $CO_2$ reduction for 12 hours at 250 °C. Growth of the peak associated with linearly-bound CO (dashed line, ~2,060 $cm^{-1}$) is indicative of the formation of metal nanoparticles at the expense of metal single atoms.*

### *3.5 The effects of amine group positioning*

When designing catalytic surfaces with different binding sites (e.g., metal and acid sites), spacing between the sites is often an important factor for bifunctional effects.[54,55] This has recently been proven the case for enzyme-inspired bifunctional peptide catalysts as well as for Pt-containing large-pore zeolites, which both benefited from nanoscale proximity of different sites.[56,57] However, a growing body of work has shown that close proximity between sites is not always beneficial, particularly for metal-acid bifunctional catalysts.[55,58,59] To test the sensitivity to small changes in $Rh_1$/amine group intimacy, we deposited $C_1NH_2PA$, $C_3NH_2PA$, and $C_{12}NH_2PA$ onto $Rh_1/TiO_2$. These ligands have one, three, and twelve methylene groups between the PA head group and terminal amine, respectively, as opposed to the two methylenes of $C_2NH_2PA$. For the short chain PAs, the degree of organization in the organic tails is expected to be low, such that various conformations are possible. Longer-chain PAs such as $C_{12}NH_2PA$, however, have sufficient dispersion interactions that they form ordered layers, as demonstrated for example by the position of the $CH_2$ asymmetric stretching frequency in infrared spectroscopy studies.[14,18] In

the present study, we observed an asymmetric $CH_2$ stretching peak at 2918 $cm^{-1}$ for $C_{12}NH_2PA@Rh_1/TiO_2$ (Figure S11) consistent with a well-organized monolayer.[18]

Amino-PA tail length significantly affected $H_2/D_2$ scrambling (Figure 7a), suggesting a strong sensitivity of molecular hydrogen dissociation active site density tail functionality. Surprisingly, both the longer and shorter PA tails resulted in less apparent site blocking compared to $C_2NH_2PA$. The $C_1NH_2PA$- and $C_3NH_2PA$-modified samples showed ~3× and ~6× more available Rh sites than $C_2NH_2PA$. The long-chain $C_{12}NH_2PA$ also resulted in a statistically significant increase in the $H_2/D_2$ scrambling rate. This further indicates that loss of Rh sites was an effect of the PA tails rather than the phosphonate head group, as discussed above. We speculate that $C_1NH_2PA$ tails may not be long enough to block sites as consistently as $C_2NH_2PA$ due to diminished steric constraints. Previous studies have shown that surface-bound ligands with longer tails tend to orient themselves more normal to the catalyst surface, hypothetically providing more well-defined channels for reactants to diffuse through.[31] This could explain why less site blocking was observed for $C_3NH_2PA$ than the shorter-tailed $C_2NH_2PA$.

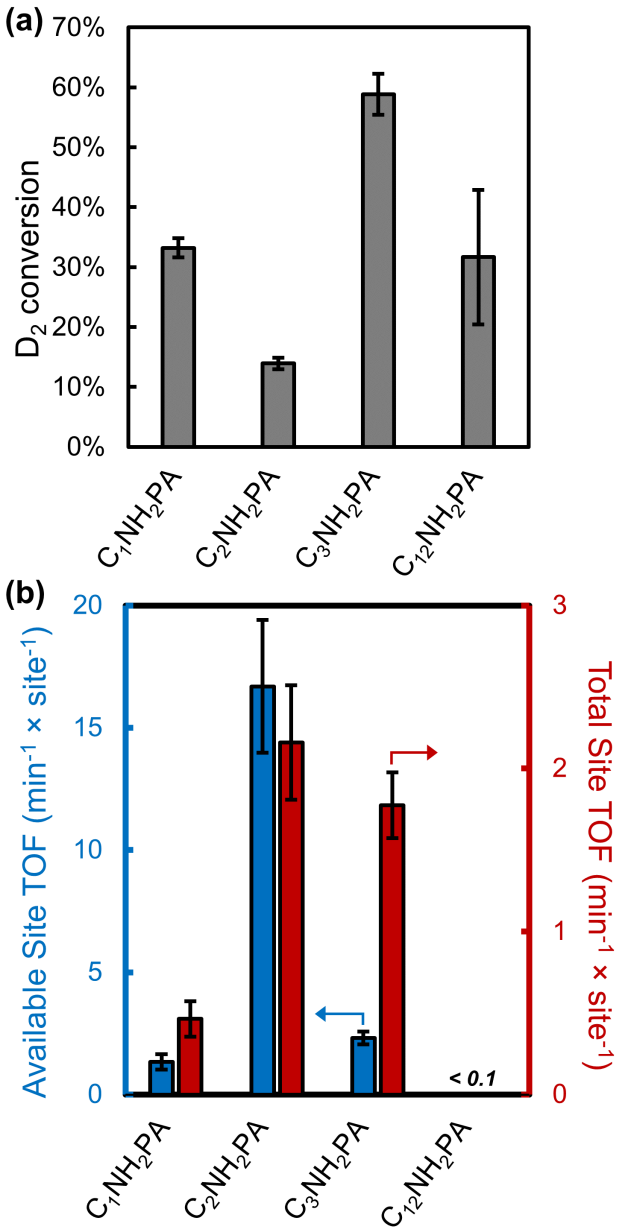


*Figure 7.* ***Effects of alkyl spacer length on site availability and activity****. (a) $D_2$ conversion during $H_2/D_2$ scrambling experiments for $Rh_1/TiO_2$ modified with different amine-functionalized PAs. $D_2$ was introduced by 1mL injections while flowing constant 20% $H_2$/Ar. (b) Turnover frequencies for $CO_2$ reduction to CO based on available sites (blue, left axis) and mass activity based on total Rh loading regardless of blocking (red, right axis). Available sites calculated based on $H_2/D_2$ scrambling conversion.*

$C_1NH_2PA$- and $C_3NH_2PA$-modified $Rh_1/TiO_2$ were also tested for RWGS activity at 250 °C with the same flow conditions as the previous experiments. Figure 7b shows both the available-site TOF (left axis) and total-site rate (right axis) for catalysts with these modifiers. Without normalizing by available sites, activity was not significantly different between $C_2NH_2PA$- and $C_3NH_2PA$-modified samples, whereas $C_1NH_2PA$ produced a nearly 5× decrease in total activity. Normalizing by available sites, TOFs for the $C_2NH_2PA$-modified catalysts showed 13× and 7×

improvements over those with $C_1NH_2PA$ and $C_3NH_2PA$, respectively. This was surprising for $Rh_1/TiO_2@C_3NH_2PA$, as DFT calculations of functionalized thiolates have demonstrated the ability of organic ligands to bend, forming gauche defects, in order to accommodate ligand-adsorbate interactions.[7] However, these calculations did not consider the potential tradeoff from disturbing ligand-ligand interactions, nor the entropic penalty for creating a sterically rigid adsorption geometry.

The geometric factors that lead to high site-blocking in the $C_2NH_2PA$-modified samples may also be responsible for the high specific activity on those same catalysts. We propose that there is close proximity between the $C_2NH_2PA$ tails and $Rh_1$ sites – so much so as to apparently cause significant site blocking. This intimacy between $Rh_1$ sites and terminal amines appears to be beneficial towards RWGS activity on a per-site basis, as these amine groups provide the only $CO_2$ adsorption sites on the catalyst surface while the $Rh_1$ sites are the only species capable of dissociating $H_2$. Unlike cases where bifunctional sites can catalyze different reaction steps far from each other, relying on diffusion of intermediates, site proximity appears to play an important role in this system.

One indication of the importance of site proximity is that $Rh_1/TiO_2@C_{12}NH_2PA$ was found to be completely inactive for $CO_2$ reduction, producing no detectable CO or $CH_4$ at 250 °C (Figure 7b). This was despite the fact that both active hydrogenation and $CO_2$ binding sites were still present in high abundance on the catalyst; as noted above, $Rh_1/TiO_2@C_{12}NH_2PA$ had higher activity for $H_2/D_2$ scrambling that the $C_2NH_2PA$-modified catalyst. Furthermore, $CO_2$ DRIFTS experiments (Figure S12) showed that the $C_{12}NH_2PA$-modified catalyst bound $CO_2$ similarly to other amino-PA-modified samples. Thus, although the amine group for $C_{12}NH_2PA$ is remote from the surface-tethering phosphonate group, it is still capable of adsorbing $CO_2$. We therefore conclude that the complete lack of activity is due to the significantly greater distance between the $Rh_1$ sites and the $C_{12}NH_2PA$'s terminal amine. Thus, for the PA-modified catalysts, proximity between the amine function and the Rh active site is critical for reaction. However, we note that other factors (such as the electronic and entropic effects on CO adsorption discussed above) appear to play a role in determining reactivity of PA-modified systems.

It is worth pointing out that the observed sensitivity of RWGS rates to the positioning of amine functions on the PA was much higher for the SAC $Rh_1/TiO_2$ (the current study) than the supported nanoparticle catalyst $Pt/TiO_2$ (published previously).[13] Moreover, the nearly complete suppression of RWGS activity for alkyl phosphonic acids and long chain amines (while short chain amines show high activity) is a tail-dependent feature that, to our knowledge, has not been reported for organic-modified heterogeneous catalysts. This higher degree of sensitivity is in line with the more precise structuring of the active site that is possible for single atom catalysts. Thus, while much work is needed to understand how to position organic functional groups for optimal reactivity down desired pathways, this manuscript reveals that the use of organic monolayers to modify SACs holds the promise to tailor active sites for high reactivity. Such tailoring of reactive environments could also be used in emerging applications that go beyond steady state catalytic reactions, such as "reactive capture" concepts.[60]

## 4. CONCLUSIONS

In conclusion, $Rh_1/TiO_2$ SACs were modified with various PA SAMs, characterized with probe molecule DRIFTS, XAS, and $H_2/D_2$ scrambling, and tested for RWGS activity. XAS studies showed that the deposited PAs were located in close proximity to $Rh_1$ sites and withdrew electron density from the metal atom, and DFT model structures suggest the formation of Rh–O–P bonds. Although PAs blocked $CO_2$ adsorption sites on the $TiO_2$ surface, amine-functionalization of the ligands partially restored $CO_2$ adsorption. Deposition of PAs decreased the apparent density of accessible Rh sites, most likely due to site blocking by tail groups. $C_2NH_2PA$-modified catalysts saw significant improvements in specific activity for RWGS, as well as improved selectivity towards CO at conditions where methanation occurred on the unmodified SAC. Though the deposition of unfunctionalized $C_3PA$ led to a complete loss of activity due to the inability of $CO_2$ to adsorb, removal of the alkyl tails via oxidation resulted in the recovery of catalytic activity. Finally, tail length of amino-PAs was found to play a significant role in both $Rh_1$ site blocking and catalytic activity, with long-chain $C_{12}NH_2PA$ modifiers showing no detectable RWGS activity. Overall, this work shows that the reactivity of single atom catalysts is highly sensitive to the positioning of functional groups that are installed in the near-surface environment. This sensitivity is much greater than that observed in previous studies of supported nanoparticle catalysts, suggesting that organic modification of SACs may provide a unique platform for tailoring the active site environment.

## AUTHOR INFORMATION


### Corresponding Author

*Email: will.medlin@colorado.edu


### Author Contributions

The manuscript was written through contributions of all authors. All authors have given approval to the final version of the manuscript.

### Notes

The authors declare no competing financial interest.

## SUPPORTING INFORMATION

Supporting Information includes DRIFTS and NMR spectra for organic characterization catalysts, CO and $CO_2$ DRIFTS for probing binding sites on the various catalysts, DFT-computed structures for phosphonate-modified $Rh_1/TiO_2$, RWGS turnover frequencies for various catalysts measured at 250°C, stability tests for coated and uncoated catalysts, and extensive discussion of XAS analysis.

The Supporting Information is available free of charge on the ACS Publications website.

## ACKNOWLEDGMENTS

This work was supported by the Department of Energy, Office of Science, Basic Energy Sciences Program, Chemical Sciences, Geosciences, and Biosciences Division [Grant No. DE-SC0005239]. This work utilized the Summit supercomputer, which is supported by the National Science Foundation (awards ACI-1532235 and ACI-1532236), the University of Colorado Boulder, and Colorado State University. The Summit supercomputer is a joint effort of the University of Colorado Boulder and Colorado State University. The authors gratefully acknowledge Casey Davis, Brandon Oliphant, and Qing Ma for their assistance with beamline experiments and Sean Najmi for performing $^{31}$P NMR measurements.

## REFERENCES

(1) Burch, R.; Breen, J. P.; Meunier, F. C. A Review of the Selective Reduction of NOx with Hydrocarbons under Lean-Burn Conditions with Non-Zeolitic Oxide and Platinum Group Metal Catalysts. *Appl. Catal. B Environ.* **2002**, *39* (4), 283–303.

(2) Ghenciu, A. F. Review of Fuel Processing Catalysts for Hydrogen Production in PEM Fuel Cell Systems. *Curr. Opin. solid state Mater. Sci.* **2002**, *6* (5), 389–399.

(3) Liotta, L. F. Catalytic Oxidation of Volatile Organic Compounds on Supported Noble Metals. *Appl. Catal. B Environ.* **2010**, *100* (3–4), 403–412.

(4) Mark, L. O.; Cendejas, M. C.; Hermans, I. The Use of Heterogeneous Catalysis in the Chemical Valorization of Plastic Waste. *ChemSusChem* **2020**, *13* (22), 5808–5836.

(5) Sabatier. *La Catalyse En Chimie Organique*; Nouveau Monde, 2013. https://doi.org/10.14375/NP.9782369430186.

(6) Pérez-Ramírez, J.; López, N. Strategies to Break Linear Scaling Relationships. *Nat. Catal.* **2019**, *2* (11), 971–976. https://doi.org/10.1038/s41929-019-0376-6.

(7) Jenkins, A. H.; Musgrave, C. B.; Medlin, J. W. Altering Linear Scaling Relationships on Metal Catalysts via Ligand-Adsorbate Hydrogen Bonding. *J. Phys. Chem. C* **2021**, *125* (43), 23791–23802. https://doi.org/10.1021/acs.jpcc.1c07550.

(8) Liu, J. Catalysis by Supported Single Metal Atoms. *ACS Catal* 34–59 **2017**, *7* (1) 34-59. https://doi.org/10.1021/acscatal.6b01534.

(9) Darby, M. T.; Stamatakis, M.; Michaelides, A.; Sykes, E. C. H. Lonely Atoms with Special Gifts: Breaking Linear Scaling Relationships in Heterogeneous Catalysis with Single-Atom Alloys. *J. Phys. Chem. Lett.* **2018**, *9* (18), 5636–5646. https://doi.org/10.1021/acs.jpclett.8b01888.

(10) Lee, S.; Patra, A.; Christopher, P.; Vlachos, D. G.; Caratzoulas, S. Theoretical Study of Ethylene Hydroformylation on Atomically Dispersed Rh/Al2O3Catalysts: Reaction Mechanism and Influence of the ReOxPromoter. *ACS Catal.* **2021**, *11* (15), 9506–9518. https://doi.org/10.1021/acscatal.1c00705.

(11) Asokan, C.; Yang, Y.; Dang, A.; Getsoian, A.; Christopher, P. Low-Temperature Ammonia Production during NO Reduction by CO Is Due to Atomically Dispersed Rhodium Active Sites. *ACS Catal.* **2020**, *10* (9), 5217–5222. https://doi.org/10.1021/acscatal.0c01249.

(12) Zhang, J.; Ellis, L. D.; Wang, B.; Dzara, M. J.; Sievers, C.; Pylypenko, S.; Nikolla, E.; Medlin, J. W. Control of Interfacial Acid–Metal Catalysis with Organic Monolayers. *Nat. Catal.* **2018**, *1* (2), 148–155. https://doi.org/10.1038/s41929-017-0019-8.

(13) Zhang, J.; Deo, S.; Janik, M. J.; Medlin, J. W. Control of Molecular Bonding Strength on Metal Catalysts with Organic Monolayers for CO2 Reduction. *J. Am. Chem. Soc.* **2020**. https://doi.org/10.1021/jacs.9b12980.

(14) Jenkins, A. H.; Medlin, J. W. Controlling Heterogeneous Catalysis with Organic Monolayers on Metal Oxides. *Acc. Chem. Res.* **2021**, *54* (21), 4080–4090. https://doi.org/10.1021/acs.accounts.1c00469.

(15) Zhang, J.; Asokan, C.; Zakem, G.; Christopher, P.; Medlin, J. W. Enhancing Sintering Resistance of Atomically Dispersed Catalysts in Reducing Environments with Organic Monolayers. *Green Energy Environ.* **2021**, No. xxxx, 4–10. https://doi.org/10.1016/j.gee.2021.01.022.

(16) Zakem, G.; Ro, I.; Finzel, J.; Christopher, P. Support Functionalization as an Approach for Modifying Activation Entropies of Catalytic Reactions on Atomically Dispersed Metal Sites. *J. Catal.* **2021**, *404*, 883–896. https://doi.org/10.1016/j.jcat.2021.07.030.

(17) DeRita, L.; Dai, S.; Lopez-Zepeda, K.; Pham, N.; Graham, G. W.; Pan, X.; Christopher, P. Catalyst Architecture for Stable Single Atom Dispersion Enables Site-Specific Spectroscopic and Reactivity Measurements of CO Adsorbed to Pt Atoms, Oxidized Pt Clusters, and Metallic Pt Clusters on TiO2. *J. Am. Chem. Soc.* **2017**, *139* (40), 14150–14165. https://doi.org/10.1021/jacs.7b07093.

(18) Ellis, L. D.; Trottier, R. M.; Musgrave, C. B.; Schwartz, D. K.; Medlin, J. W. Controlling the Surface Reactivity of Titania via Electronic Tuning of Self-Assembled Monolayers. *ACS Catal.* **2017**, *7* (12), 8351–8357. https://doi.org/10.1021/acscatal.7b02789.

(19) Kresse, G.; Hafner, J. Ab Initio Molecular Dynamics for Liquid Metals. *Phys. Rev. B* **1993**, *47* (1), 558–561. https://doi.org/10.1103/PhysRevB.47.558.

(20) Kresse, G.; Hafner, J. Ab Initio Molecular-Dynamics Simulation of the Liquid-Metalamorphous- Semiconductor Transition in Germanium. *Phys. Rev. B* **1994**, *49* (20), 14251–14269. https://doi.org/10.1103/PhysRevB.49.14251.

(21) Kresse, G.; Furthmüller, J. Efficient Iterative Schemes for Ab Initio Total-Energy Calculations Using a Plane-Wave Basis Set. *Phys. Rev. B* **1996**, *54* (16), 11169–11186. https://doi.org/10.1021/acs.jpca.0c01375.

(22) Kresse, G.; Furthmüller, J. Efficiency of Ab-Initio Total Energy Calculations for Metals and Semiconductors Using a Plane-Wave Basis Set. *Comput. Mater. Sci.* **1996**, *6* (1), 15–50. https://doi.org/10.1016/0927-0256(96)00008-0.

(23) Blöchl, P. E. Projector Augmented-Wave Method. *Phys. Rev. B* **1994**, *50* (24), 17953–

17979. https://doi.org/10.1103/PhysRevB.50.17953.

(24) Sun, J.; Ruzsinszky, A.; Perdew, J. Strongly Constrained and Appropriately Normed Semilocal Density Functional. *Phys. Rev. Lett.* **2015**, *115* (3), 1–6. https://doi.org/10.1103/PhysRevLett.115.036402.

(25) Henkelman, G.; Arnaldsson, A.; Jónsson, H. A Fast and Robust Algorithm for Bader Decomposition of Charge Density. *Comput. Mater. Sci.* **2006**, *36* (3), 354–360. https://doi.org/10.1016/j.commatsci.2005.04.010.

(26) Yang, C.; Garl, C. W. Infrared Studies of Carbon Monoxide Chemisorbed on Rhodium. *J. Phys. Chem.* **1957**, *61* (11), 1504–1512.

(27) Yates Jr., J. T.; Duncan, T. M.; Worley, S. D.; Vaughan, R. W. Infrared Spectra of Chemisorbed CO on Rh. *J. Chem. Phys.* **1979**, *70* (1219).

(28) Horch, S.; Lorensen, H. T.; Helveg, S.; Lægsgaard, E.; Stensgaard, I.; Jacobsen, K. W.; Nørskov, J. K.; Besenbacher, F. Enhancement of Surface Self-Diffusion of Platinum Atoms by Adsorbed Hydrogen. *Nature* **1999**, *398*, 134–136.

(29) Parkinson, G. S.; Novotny, Z.; Argentero, G.; Schmid, M.; Pavelec, J.; Kosak, R.; Blaha, P.; Diebold, U. Carbon Monoxide-Induced Adatom Sintering in a Pd–Fe3O4 Model Catalyst. *Nat. Mater.* **2013**, *12*, 724–728.

(30) Matsubu, J. C.; Yang, V. N.; Christopher, P. Isolated Metal Active Site Concentration and Stability Control Catalytic CO2 Reduction Selectivity. *J. Am. Chem. Soc.* **2015**, *137* (8), 3076–3084. https://doi.org/10.1021/ja5128133.

(31) Marshall, S. T.; O'Brien, M.; Oetter, B.; Corpuz, A.; Richards, R. M.; Schwartz, D. K.; Medlin, J. W. Controlled Selectivity for Palladium Catalysts Using Self-Assembled Monolayers. *Nat. Mater.* **2010**, *9* (10), 853–858. https://doi.org/10.1038/nmat2849.

(32) Jenkins, A. H.; Musgrave, C. B.; Medlin, J. W. Enhancing Au/TiO 2 Catalyst Thermostability and Coking Resistance with Alkyl Phosphonic-Acid Self-Assembled Monolayers. *ACS Appl. Mater. Interfaces* **2019**, *11* (44), 41289–41296. https://doi.org/10.1021/acsami.9b13170.

(33) Geldof, D.; Tassi, M.; Carleer, R.; Adriaensens, P.; Roevens, A.; Meynen, V.; Blockhuys, F. Binding Modes of Phosphonic Acid Derivatives Adsorbed on TiO2 Surfaces: Assignments of Experimental IR and NMR Spectra Based on DFT/PBC Calculations. *Surf. Sci.* **2017**, *655*, 31–38.

(34) Guerrero, G.; Mutin, P. H.; Vioux, A. Anchoring of Phosphonate and Phosphinate Coupling Molecules on Titania Particles. *Chem. Mater.* **2001**, *13* (11), 4367–4373.

(35) Tang, Y.; Asokan, C.; Xu, M.; Graham, G. W.; Pan, X.; Christopher, P.; Li, J.; Sautet, P. Rh Single Atoms on TiO2 Dynamically Respond to Reaction Conditions by Adapting Their Site. *Nat. Commun.* **2019**, *10* (1), 1–11. https://doi.org/10.1038/s41467-019-12461-6.

(36) Wang, K.; Cao, M.; Lu, J.; Lu, Y.; Lau, C. H.; Zheng, Y.; Fan, X. Operando DRIFTS-MS Investigation on Plasmon-Thermal Coupling Mechanism of CO2 Hydrogenation on

Au/TiO2: The Enhanced Generation of Oxygen Vacancies. *Appl. Catal. B Environ.* **2021**, *296*, 120341. https://doi.org/10.1016/j.apcatb.2021.120341.

(37) Wilfong, W. C.; Srikanth, C. S.; Chuang, S. S. C. In Situ ATR and DRIFTS Studies of the Nature of Adsorbed CO2 on Tetraethylenepentamine Films. *ACS Appl. Mater. Interfaces* **2014**, *6*, 13617–13626.

(38) Bacsik, Z.; Ahlsten, N.; Ziadi, A.; Zhao, G.; Garcia-Bennett, A. E.; Martin-Matute, B.; Hedin, N. Mechanisms and Kinetics for Sorption of CO2 on Bicontinuous Mesoporous Silica Modified with N-Propylamine. *Langmuir* **2011**, *27*, 11118–11128.

(39) Ma, T. Y.; Lin, X. Z.; Zhang, X. J.; Yuan, Z. Y. High Surface Area Titanium Phosphonate Materials with Hierarchical Porosity for Multi-Phase Adsorption. *New J. Chem.* **2010**, *34* (6), 1209–1216. https://doi.org/10.1039/b9nj00775j.

(40) Tian-Yi, M.; Lin, X. Z.; Yuan, Z. Y. Cubic Mesoporous Titanium Phosphonates with Multifunctionality. *Chem. - A Eur. J.* **2010**, *16* (28), 8487–8494. https://doi.org/10.1002/chem.201000364.

(41) Rehr, J. J.; Albers, R. Theoretical Approaches to X-Ray Absorption Fine Structure. *Revi. Mod. Phys.* **2000**, *72* (3), 621.

(42) Rehr, J. J.; Kas, J. J.; Prange, M. P.; Sorini, A. P.; Takimoto, Y.; Vila, F. Ab Initio Theory and Calculations of X-Ray Spectra. *Comptes Rendus Phys.* **2009**, *10* (6), 548–559. https://doi.org/10.1016/j.crhy.2008.08.004.

(43) Huizing, T.; Van Grondelle, J.V.; Prins, R. A Temperature Programmed Reducation Study of Pt on $Al_2O_3$ and $TiO_2$. *Appl. Catal*. **1984**, *10*, 199-213.

(44) Zhang, J.; Wang, B.; Nikolla, E.; Medlin, J.W. Directing Reaction Pathways through Controlled Reactant Binding at Pd–$TiO_2$ Interfaces. *Angew. Chem. Int. Ed*. **2017**, *129*, 6694-6698.

(45) Finzel, J.; Sanroman Gutierrez, K. M.; Hoffman, A. S.; Resasco, J.; Christopher, P.; Bare, S. R. Limits of Detection for EXAFS Characterization of Heterogeneous Single-Atom Catalysts. *ACS Catal*. **2023**, *13* (9), 6462-6473.

(46) Gogate, M. R.; Davis, R. J. X-Ray Absorption Spectroscopy of an Fe-Promoted Rh/TiO2 Catalyst for Synthesis of Ethanol from Synthesis Gas. *ChemCatChem* **2009**, *1* (2), 295–303. https://doi.org/10.1002/cctc.200900104.

(47) Bai, S.; Liu, F.; Huang, B.; Li, F.; Lin, H.; Wu, T.; Sun, M.; Wu, J.; Shao, Q.; Xu, Y.; Huang, X. High-Efficiency Direct Methane Conversion to Oxygenates on a Cerium Dioxide Nanowires Supported Rhodium Single-Atom Catalyst. *Nat. Commun.* **2020**, *11* (1), 1–9. https://doi.org/10.1038/s41467-020-14742-x.

(48) Kwon, Y.; Kim, T. Y.; Kwon, G.; Yi, J.; Lee, H. Selective Activation of Methane on Single-Atom Catalyst of Rhodium Dispersed on Zirconia for Direct Conversion. *J. Am. Chem. Soc.* **2017**, *139* (48), 17694–17699. https://doi.org/10.1021/jacs.7b11010.

(49) Rice, C. A.; Worley, S. D.; Curtis, C. W.; Guin, J. A.; Tarrer, A. R. The Oxidation State of Dispersed Rh on AI2O3. *J. Chem. Phys.* **1981**, *74* (11), 6487–6497.

https://doi.org/10.1063/1.440987.

(50) Shimizu, K. I.; Oda, T.; Sakamoto, Y.; Kamiya, Y.; Yoshida, H.; Satsuma, A. Quantitative Determination of Average Rhodium Oxidation State by a Simple XANES Analysis. *Appl. Catal. B Environ.* **2012**, *111–112*, 509–514. https://doi.org/10.1016/j.apcatb.2011.11.002.

(51) Wilson, R. L.; Kemball, C.; Galwey, A. K. Catalytic Exchange of Hydrogen Sulphide and of Hydrogen with Deuterium on Disulphides of Molybdenum and Tungsten. *Trans. Faraday Soc.* **1962**, *58*, 583–592. https://doi.org/10.1039/tf9625800583.

(52) Frontera, P.; Macario, A.; Ferraro, M.; Antonucci, P. Supported Catalysts for CO2 Methanation: A Review. *Catalysts* **2017**, *7* (2), 59.

(53) Zhu, Y.; Yuk, S. F.; Zheng, J.; Nguyen, M.; Lee, M.; Szanyi, J.; Kovarik, L.; Zhu, Z.; Balasubramanian, M.; Glezakou, V.; Fulton, J. L.; Lercher, J. A.; Rousseau, R.; Gutierrez, O. Y. Environment of Metal–O–Fe Bonds Enabling High Activity in CO2 Reduction on Single Metal Atoms and on Supported Nanoparticles. *J. Am. Chem. Soc.* **2021**, *143* (14), 5540–5549.

(54) Weisz, P. B. Polyfunctional Heterogeneous Catalysis. *Adv. Catal.* **1962**, *13*, 137–190.

(55) Zecevic, J.; Vanbutsele, G.; de Jong, K. P.; Martens, J. A. Nanoscale Intimacy in Bifunctional Catalysts for Selective Conversion of Hydrocarbons. *Nature* **2015**, *528*, 245–248.

(56) Kinghorn, M. J.; Valdivia-Berroeta, G. A.; Chantry, D. R.; Smith, M. S.; Ence, C. C.; Draper, S.; Duval, J.; Masino, B.; Cahoon, S.; Flansburg, R.; Conder, C. J.; Price, J. L.; Michaelis, D. J. Proximity-Induced Reactivity and Product Selectivity with a Rationally Designed Bifunctional Peptide Catalyst. *ACS Catal.* **2017**, *7* (11), 7704–7708.

(57) Oenema, J.; Harmel, J.; Pérez Vélez, R.; Meijerink, M.; Eijsvogel, W.; Poursaeidesfahani, A.; Vlugt, T.; Zečević, J.; de Jong, K. Influence of Nanoscale Intimacy and Zeolite Micropore Size on the Performance of Bifunctional Catalysts for N-Heptane Hydroisomerization. *ACS Catal.* **2020**, *10* (23), 14245–14257.

(58) Batista, A.; Chizallet, C.; Diehl, F.; Taleb, A.; Gay, A.; Ersen, O.; Raybaud, P. Evaluating Acid and Metallic Site Proximity in Pt/γ-Al 2 O 3-Cl Bifunctional Catalysts through an Atomic Scale Geometrical Model. *Nanoscale* **2022**, *14*, 8753–8765.

(59) Samad, J.; Blanchard, J.; Sayag, C.; Louis, C.; Regalbuto, J. The Controlled Synthesis of Metal-Acid Bifunctional Catalysts: The Effect of Metal: Acid Ratio and Metal-Acid Proximity in Pt Silica-Alumina Catalysts for n-Heptane Isomerization. *J. Catal.* **2016**, *342*, 203–212.

(60) Siegel, R. E.; Pattanayak, S.; Berben, L. A. Reactive Capture of CO2: Opportunities and Challenges. *ACS Catal.* **2023**, *13* (1), 766–784. https://doi.org/10.1021/acscatal.2c05019.

Graphical Abstract